


Dual-Mode Dead-Zone-Free Double-Resonance Alignment-Based Magnetometer

He Wang¹, Teng Wu¹, Wei Xiao¹, Haidong Wang¹, Xiang Peng^{1,*}, and Hong Guo^{1,†}

State Key Laboratory of Advanced Optical Communication Systems and Networks, Department of Electronics, and Center for Quantum Information Technology, Peking University, Beijing 100871, China

 (Received 9 August 2020; revised 7 January 2021; accepted 22 January 2021; published 15 February 2021)

Magneto-optical double-resonance magnetometers are attractive candidates for sensitive measurements of magnetic fields but suffer from a fundamental problem known as the “dead zone”: certain magnetic field directions where the magnetometer loses its sensitivity. We present a dead-zone-free double-resonance magnetometer with a single linearly polarized laser, which keeps uniform signal amplitude and isotropic sensitivity among varying magnetic field directions. The isotropic magnetometer can be switched between two modes, i.e., M_z mode insensitive to phase shifts and M_x mode with a higher upper bound of bandwidth. The dead-zone-free magnetometer exhibits a magnetic field noise floor of $0.9 \text{ pT}/\sqrt{\text{Hz}}$ and $1.2 \text{ pT}/\sqrt{\text{Hz}}$ in M_z and M_x modes, respectively. The proposed double-resonance magnetometer, benefiting from its compact single-beam structure, isotropic sensitivity, and capability of dual modes, would be useful for high-sensitivity magnetic field measurements in mobile applications.

DOI: [10.1103/PhysRevApplied.15.024033](https://doi.org/10.1103/PhysRevApplied.15.024033)

I. INTRODUCTION

Optically pumped magnetometers (OPMs), with sensitivity up to subfemtotesla [1,2] and being comparable with the low-temperature superconducting quantum interference device (SQUID) magnetometers, have wide applications in magnetic field sensing [3], such as biomagnetic measurements [4–6], fundamental physics [7,8], mapping the geomagnetic field [9], and field measurements in space [10]. Traditionally, scalar OPMs measure the precession frequency of macroscopic atomic magnetic moments, which are created by a resonant polarized light, in the presence of a finite magnetic field (the bias field). The Larmor precession frequency ω_0 is proportional to the bias-field strength B_0 . A transverse rf magnetic field (much weaker than the bias field), corotating with macroscopic atomic magnetic moments, is applied to induce transitions between the magnetic sublevels and modifies the optical property of the atomic medium. Optical detection with a second probe light or the same pump light gives the scalar measurement of the bias field.

Accompanied by significant advances in magnetometer sensitivity, attempts are also made to bring OPMs into challenging environments [11]. Recently, Limes *et al.* [6] reported a portable optical gradiometric magnetometer, which has achieved a high sensitivity even in unshielded Earth’s field and is able to detect magnetic field signals from brain activities in natural environments,

making a quite significant step forward. Compared with static OPM measures, a fundamental problem becomes serious in mobile applications, known as a “dead zone”: certain magnetic field directions where the magnetometer fails to work because the resonance signal vanishes. The usage of scalar OPM in the mobile platform is one of the dominant applications of OPM because it has high sensitivity and its magnetic field readings are relatively insensitive to the magnetic field direction. However, the dead-zone effect becomes an unavoidable obstacle for OPMs in mobile platforms because the relative direction of the environment magnetic field is unknown and always changing in the mobile platform. The dead zones can be strongly suppressed by employing multiple vapor cells [12,13] or multiple sensors. However, these schemes are sensitive to the magnetic gradient. Modulating the light polarization between linear and circular polarization states [14] or two orthogonal linear polarization states [15], or adjusting the light ellipticity in intensity-modulated OPMs [16] allows the reduction of dead zones but still suffers from sensitivity losses in certain directions of the bias field. To achieve isotropic measurement of the magnetic field, the CEA-Leti proposed adjustable double-resonance alignment-based magnetometers (DRAMs), in which the light linear polarization and the rf field are adjusted and fixed at 90° with respect to the bias field [17–19]. These schemes are based on M_x configurations. Here, M_x and M_z classifications, in which the transverse and longitudinal atomic multipole moments are measured, respectively, when the quantization axis is along the direction of the bias field, are artificial concepts

*xiangpeng@pku.edu.cn

†hongguo@pku.edu.cn

but retained for convenience [20,21]. Our group developed an isotropic intensity-modulated OPM by adjusting the light linear polarization [22]. However, the readings of intensity-modulated and M_x OPMs are sensitive to the phase of detected signals. Previously, most theoretical [21,23], experimental [24,25], and practical [18,26] works about the DRAM are focused on the M_x type while the M_z -type DRAMs are rarely studied [27]. The DRAMs in M_z mode, which do not suffer from systematic errors caused by the phase shift of detected signals and thus have high accuracy [20], remain worthy of being investigated.

In this paper, we present analytical expressions for the full spectra produced by a single-beam DRAM in arbitrary magnetic field geometries. Previous work on such resonance signals [21,23] was limited to the first- and second-harmonic components of the DRAM. We extend previous work and demonstrate theoretically and experimentally that the spectra contain sufficient information to realize a dead-zone-free DRAM. The dead-zone-free DRAM not only is suitable for measuring magnetic fields with arbitrarily directions, but also can be operated optionally in M_x or M_z mode. The error signal can be directly derived from the first-harmonic component to maintain the light linear polarization and the rf field to be perpendicular with respect to the bias field, which keeps uniform sensitivity of the DRAM among arbitrary magnetic field directions. Our methods open interesting insights for isotropic high-sensitivity OPMs operated in the mobile platform such as an aircraft and a spacecraft. In addition, the single-beam structure is suitable for the miniaturized or chip-scale OPMs [18,28].

The paper is organized as follows. In Sec. II, we describe the theoretical model and derive analytical expressions for the full spectra produced by the single-beam DRAM. In Sec. III, we present the experimental setup of the dual-mode single-beam isotropic DRAM with ^4He atoms and experimental results. Section IV contains the conclusions.

II. THEORETICAL MODEL

The geometry of a single-beam DRAM is shown in Fig. 1, which is fully determined by the bias field \mathbf{B}_0 , the light linear polarization ϵ , and the rf field \mathbf{B}_1 . Note that the resonance signals produced by a resonant linearly polarized light are independent of the light propagation direction. \mathbf{B}'_1 is the projection of the rf field onto the x - y plane. Only the component of the rf field corotating with atomic alignment is reserved under the rotating-wave approximation. The angular dependence of the resonance signal is determined by the angles φ and θ , while the angle α denotes the phase shift between the rotating rf field and the atomic alignment.

The density matrix $\hat{\rho}$ of an atomic state with angular momentum F can be decomposed in the basis of

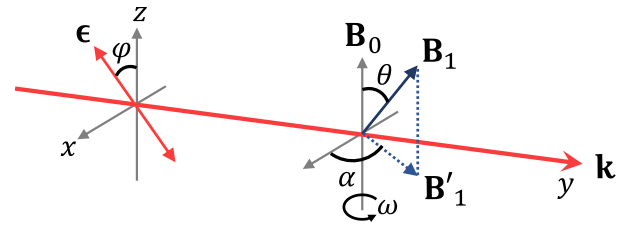


FIG. 1. Geometry of the DRAM. The quantization axis is along the direction of the bias field \mathbf{B}_0 . The light propagates along the y direction at an angle φ with respect to the bias field \mathbf{B}_0 . θ is the angle between the rf field \mathbf{B}_1 and the bias field \mathbf{B}_0 . \mathbf{B}'_1 is the projection of the rf field onto the x - y plane. The rf field rotates at frequency ω , with an initial phase α .

irreducible tensor operators

$$\hat{\rho} = \sum_{k=0}^{2F} \sum_{q=-k}^k \rho_q^{(k)} \hat{T}_q^{(k)}, \quad (1)$$

where $\rho_q^{(k)} = (-1)^q \text{Tr}(\hat{\rho} \hat{T}_{-q}^{(k)})$ are the atomic multipole moments, of which the $k=1$ components represent the orientation while the $k=2$ components describe the alignment. $\hat{T}_q^{(k)}$ is the irreducible tensor operators with order k . $\rho_0^{(k)}$ and $\rho_{q \neq 0}^{(k)}$ are longitudinal and transverse multipole moments, respectively. The linearly polarized light produces spin alignment in atoms with $F \geq 1$, and one can define a column matrix $M \equiv (\rho_{-2}^{(2)} \rho_{-1}^{(2)} \rho_0^{(2)} \rho_1^{(2)} \rho_2^{(2)})^T$. The theoretical model is based on a three-step approach (pump, precession, probe) [29], which is in the assumption of low light power. In the first step, one needs only to know the created spin polarization without knowing the specific optical-pumping process. In the second step, the initial alignment evolves towards a steady state under the combined effect of the magnetic field and the relaxation process. In the third step, the optical property of the polarized atomic medium is detected by recording the transmitted light power. This approach has been introduced to derive analytical expressions for the time-dependent resonance signals of the DRAM in Refs. [21,23], while the time-independent part is addressed in this paper to develop a M_z magnetometer.

The electric dipole transitions only couple to the atomic multipole moments with orders $k=1$ and $k=2$ [30]. When the light linear polarization is parallel to the quantization axis, the light-absorption operator is proportional to $\hat{T}_0^{(2)}$ and the equilibrium state can be written as $M_{\text{ini}} = (0 \ 0 \ m_p \ 0 \ 0)^T$, where $m_p = \Gamma_p / (\sqrt{6}\Gamma)$ is the longitudinal multipole moment with Γ_p being the optical pumping rate and Γ being the total relaxation rate [31]. A rotation of $-\varphi$ around the y axis and a rotation of ωt around the new z axis transform the $\hat{T}_0^{(2)}$ operator to a new operator whose components can be written as a column matrix M_{rot} in the

rotating frame,

$$M_{\text{rot}} = (E_{-2}^{(2)} \quad E_{-1}^{(2)} \quad E_0^{(2)} \quad E_1^{(2)} \quad E_2^{(2)})^T, \quad (2)$$

where

$$E_{-2}^{(2)} = \frac{\sqrt{6}}{4} e^{-2i\omega t} \sin^2 \varphi, \quad (3a)$$

$$E_{-1}^{(2)} = \frac{\sqrt{6}}{4} e^{-i\omega t} \sin 2\varphi, \quad (3b)$$

$$E_0^{(2)} = \frac{1}{2} (3 \cos^2 \varphi - 1), \quad (3c)$$

$$E_1^{(2)} = -\frac{\sqrt{6}}{4} e^{i\omega t} \sin 2\varphi, \quad (3d)$$

$$E_2^{(2)} = \frac{\sqrt{6}}{4} e^{2i\omega t} \sin^2 \varphi. \quad (3e)$$

When the magnetic field is finite, i.e., $B_0 \gg \Gamma/\gamma$ with γ being the gyromagnetic ratio, the transverse component will relax to zero and only the longitudinal alignment component is reserved in the equilibrium state [23]

$$M_{\text{eq}} = m_p \left(0 \quad 0 \quad \frac{3 \cos^2 \varphi - 1}{2} \quad 0 \quad 0 \right)^T. \quad (4)$$

The evolution of atomic multipole moments follows the below equation in the rotating frame: [23]

$$\frac{dM}{dt} = \mathbb{O}M + \Gamma (M_{\text{eq}} - M), \quad (5)$$

where the matrix \mathbb{O} is

$$\mathbb{O} = i \begin{pmatrix} -2\Delta & \omega_1 p_- & 0 & 0 & 0 \\ \omega_1 p_+ & -\Delta & \sqrt{\frac{3}{2}} \omega_1 p_- & 0 & 0 \\ 0 & \sqrt{\frac{3}{2}} \omega_1 p_+ & 0 & \sqrt{\frac{3}{2}} \omega_1 p_- & 0 \\ 0 & 0 & \sqrt{\frac{3}{2}} \omega_1 p_+ & \Delta & \omega_1 p_- \\ 0 & 0 & 0 & \omega_1 p_+ & 2\Delta \end{pmatrix}, \quad (6)$$

where $p_{\pm} = \exp(\pm\alpha)$ is the phase factor, $\omega_0 = \gamma B_0$ is the Larmor frequency, $\Delta = \omega - \omega_0$ is the frequency detuning, and ω_1 is the Rabi frequency of the rf field. Only the component of the rf field perpendicular to the bias field will induce transitions between the magnetic sublevels, and we have $\omega_1 = \gamma B'_1 = \gamma B_1 \sin \theta$.

The linear absorption coefficient κ of the light coupled to an electric dipole transition can be written as [32]

$$\kappa \propto \sum_{q=-2}^2 (-1)^q E_{-q}^{(2)} \rho_q^{(2)}, \quad (7)$$

where $\rho_q^{(2)}$ are from the steady-state solutions ($dM/dt = 0$) of Eq. (5). Then, the DRAM signal, which is normalized to

m_p , can be written as

$$S = S_0 + S_{\omega}(t) + S_{2\omega}(t), \quad (8)$$

with three parts

$$S_0 = h_{\text{dc}}(\varphi) - A_{\text{dc}}, \quad (9a)$$

$$S_{\omega}(t) = D_{\omega} \cos(\omega t - \alpha) - A_{\omega} \sin(\omega t - \alpha), \quad (9b)$$

$$S_{2\omega}(t) = A_{2\omega} \cos(2\omega t - 2\alpha) + D_{2\omega} \sin(2\omega t - 2\alpha). \quad (9c)$$

For simplicity, we define $G = \omega_1/\Gamma$ and $x = \Delta/\Gamma$. G^2 is the effective rf saturation parameter [21]. The absorptive and dispersive components are given by

$$A_{\text{dc}} = \frac{3G^2 (1 + 4x^2 + G^2) h_{\text{dc}}(\varphi)}{(1 + x^2 + G^2) (1 + 4x^2 + 4G^2)}, \quad (10a)$$

$$A_{\omega} = \frac{G (1 + 4x^2 + G^2) h_{\omega}(\varphi)}{(1 + x^2 + G^2) (1 + 4x^2 + 4G^2)}, \quad (10b)$$

$$D_{\omega} = \frac{xG (1 + 4x^2 - 2G^2) h_{\omega}(\varphi)}{(1 + x^2 + G^2) (1 + 4x^2 + 4G^2)}, \quad (10c)$$

$$D_{2\omega} = \frac{3xG^2 h_{2\omega}(\varphi)}{(1 + x^2 + G^2) (1 + 4x^2 + 4G^2)}, \quad (10d)$$

$$A_{2\omega} = \frac{G^2 (1 - 2x^2 + G^2) h_{2\omega}(\varphi)}{(1 + x^2 + G^2) (1 + 4x^2 + 4G^2)}, \quad (10e)$$

with the angular dependence

$$h_{\text{dc}}(\varphi) = \frac{1}{4} (3 \cos^2 \varphi - 1)^2, \quad (11a)$$

$$h_{\omega}(\varphi) = \frac{3}{4} \sin 2\varphi (3 \cos^2 \varphi - 1), \quad (11b)$$

$$h_{2\omega}(\varphi) = \frac{3}{4} \sin^2 \varphi (1 - 3 \cos^2 \varphi). \quad (11c)$$

The expressions for the $S_{\omega}(t)$ and $S_{2\omega}(t)$ components can also be found in Refs. [21,23], while the expression for the S_0 component is presented in this paper. The time-independent signal S_0 is usually used to realize a M_z magnetometer and the two time-dependent signals $S_{\omega}(t)$, $S_{2\omega}(t)$ can be employed in realizing M_x magnetometers. For M_z magnetometers, the dependence of the S_0 signal on the detuning x has a characteristic absorptive profile. In order to track and measure the bias field, one has to modulate the rf frequency ω at a low frequency ω_m ($\omega_m < \Gamma \ll \omega_0, \omega$) and detect the observed signals at the same frequency ω_m . The frequency modulation can produce a dispersive signal and avoid low-frequency noises when detecting the observed signals. Besides, the effect of the $h_{\text{dc}}(\varphi)$ component, which is independent on x , is avoided

and only the A_{dc} component contributes to M_z magnetometers. There is an extreme value of A_{dc} amplitude even when the light linear polarization is perpendicular to the bias field (a counterintuitive behavior of second-order alignment). For M_x magnetometers, the dispersive signals D_ω and $D_{2\omega}$ are employed to track and measure the bias field. M_x and M_z magnetometers have their own advantages and both are widely used in measuring the geomagnetic field. The M_x magnetometer has a higher upper bound of bandwidth but the output values of the magnetic field are sensitive to the phase of the observed signals [seen in Eq. (9)], while the tracked frequency of a M_z magnetometer is insensitive to the signal phase but the modulation frequency ω_m (thus the relaxation rate Γ) limits its bandwidth [20].

Suppose that the light linear polarization and the rf field are parallel, i.e., $\varphi = \theta$ (referred to as the heading angle of the DRAM), the phase α is zero. The A_{dc} and $S_{2\omega}(t)$ signals have peak values around 90° , while the $S_\omega(t)$ signals are zero and feature linear dependence on θ near 90° . The dispersive components are always zero when the rf frequency is on resonance ($x = 0$). Thus, the absorptive component A_ω in the $S_\omega(t)$ signal could be used to adjust the DRAM while the A_{dc} and $S_{2\omega}(t)$ signals could be employed to measure the strength of the bias field. In addition, it can be

easily proved that the perpendicular geometry can always be reached for an arbitrarily oriented bias field even that the rf field and the light linear polarization could only be rotated in the plane of the linear polarization.

III. EXPERIMENTAL SETUP OF A DUAL-MODE DEAD-ZONE-FREE DRAM WITH ^4He ATOMS

The experimental setup is shown in Fig. 2. A fiber laser module (Koheras AdjustiK Y10) emits a linearly polarized light with frequency stabilized to the ^4He D_0 transition line ($2^3S_1 - 2^3P_0$) using a polarization spectroscopy system [33]. The light power is stabilized with an acoustic optical modulator and a proportion-integration-differentiation (PID3 in Fig. 2). A 38.4-MHz rf discharge is applied to produce metastable ^4He atoms (not shown in Fig. 2). The ^4He atoms enclosed in a cylindrical glass 70 mm long with a 50 mm diameter (at room temperature, 0.4 Torr), exposed to the bias field (about $2 \mu\text{T}$), is placed in a magnetic shield. A dual-channel lock-in amplifier (LIA, Zurich Instruments, model HF2LI) is used to derive the in-phase and quadrature components of detected signals. A voltage-controlled liquid-crystal polarization rotator (LCPR) [18], which consists of two quarter-wave plates and a liquid-crystal retarder (THORLABS, the same one as in Ref.

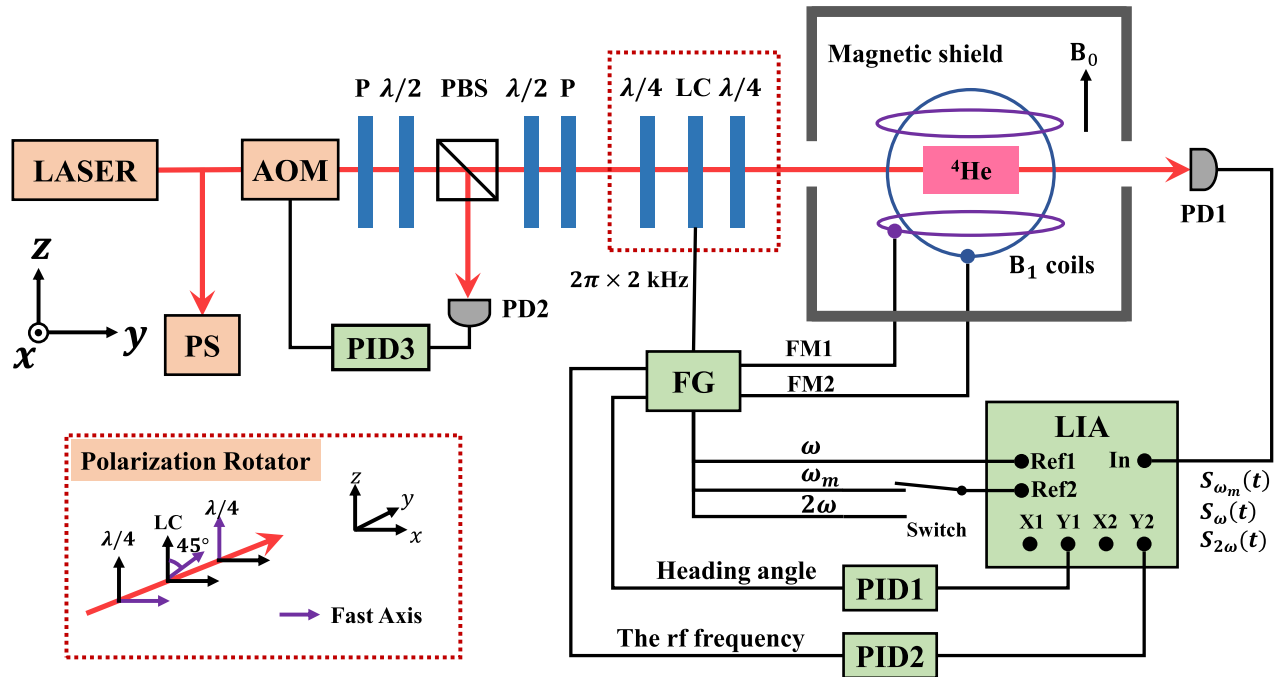


FIG. 2. Experimental setup. The polarization rotator, which rotates the light linear polarization, comprises two quarter-wave plates and a voltage-controlled liquid-crystal retarder, whose fast axes are shown in the dashed frame. Two orthogonal coils (the B_1 coils) with adjustable amplitudes are applied to rotate the direction of the rf field. The two-dimensional coils to produce the bias field B_0 on the x - z plane are not shown. The dual-channel lock-in amplifier is employed to extract the in-phase and quadrature components of detected signals. PS, polarization spectroscopy; AOM, acoustic optical modulator; P, polarizer; PBS, polarization beam splitter; PID, proportion-integration-differentiation; LC, liquid crystal; FG, function generator; FM, frequency modulation; PD, photodiode; LIA, lock-in amplifier.

[22]), is used to rotate the light linear polarization. The LCPR is driven by a $2\pi \times 2$ kHz sinusoidal signal from the function generator and the rotation angle is determined by the peak-to-peak voltage. The rotation-angle range of the LCPR is larger than 180° , which is enough for our dead-zone-free DRAM system. The response frequency range of the LCPR is from dc to 25 Hz under room temperature. Two pairs of orthogonal coils are used to adjust the rf field direction (\mathbf{B}_1 coils shown in Fig. 2).

Theoretical predictions from Eqs. (8)–(11) are based on the three-step approach, which is in the assumption of low light power ($\Gamma_p \ll \Gamma$). However, OPMs are known to perform best when Γ_p is comparable to Γ [23]. As shown in Fig. 3, the laser power has been optimized as about 3.5 mW (measured with a power meter, model THORLABS PM100D with S121C sensor) to obtain the largest slope of the dispersive signal demodulated at ω_m when the rf frequency is on resonance. The laser beam has a $1/e^2$ waist diameter of about 5 mm (approximate Gaussian profile). The pump light yields an isotropic relaxation rate and three anisotropic relaxation rates ($\Gamma_{|q|}$ for atomic multipole moments $\rho_q^{(2)}$) due to the second-order effects [34]. The difference among the three independent relaxation rates may be not negligible when the light power is high. However, the linewidth broadened by the pump light is about $2\pi \times 1$ kHz when the light power is about 3.5 mW, as shown in Fig. 3, and the final linewidth of the resonance signal is larger than $2\pi \times 4$ kHz (depends on the rf amplitude and the modulation depth). Although the light power is beyond the low-light-power assumption, we show below (Figs. 4–6) that experimental results are still in good agreement with theoretical predictions from Eqs. (8)–(11). Thus, we retain the assumption of one identical relaxation rate to obtain elegant and easy-to-understand expressions. Note that for alkali-metal atoms confined within a paraffin-coated glass cell, Ref. [24] presents that the transverse relaxation rates are quite different from the longitudinal relaxation rate even when the pump power is close to zero, and theoretical fits with three independent relaxation rates are better than with one identical relaxation rate.

The direction of the rf field can be maintained to be parallel to the light linear polarization through the following settings. Initially, both the light linear polarization and the rf field are along the z direction. Then, the light linear polarization and the rf field are always rotated with the same angle (the heading angle). We use a polynomial function of degree 5 to fit the relationship of the LCPR rotation angle versus the sinusoidal signal voltage. The deviation of the polynomial fitting from the experimental data is within $\pm 1.2^\circ$. Alternatively, a look-up table can be used to store the rotation angle versus the voltage amplitude of the sinusoidal signal. The amplitudes of the coils (\mathbf{B}_1 coils in Fig. 2) along the x and z direction are set as $B_1 \sin \varphi$, $B_1 \cos \varphi$, respectively, and then the rf field is maintained to be parallel to the light linear polarization ($\theta = \varphi$).

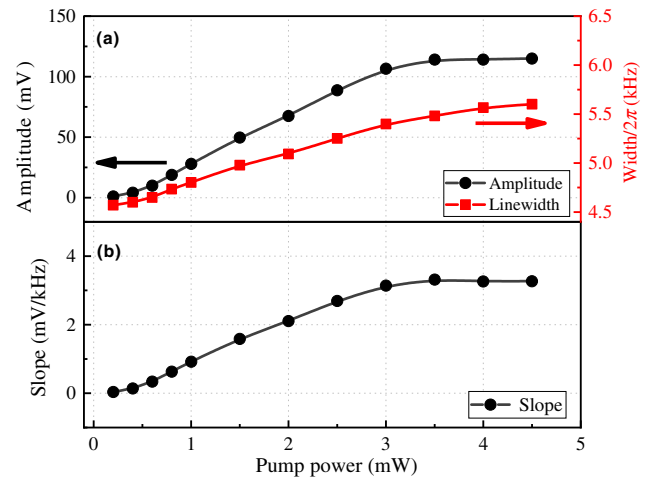


FIG. 3. Dependence of the M_z dispersive signal demodulated at ω_m on the light power. (a) Peak-to-peak amplitude (black circles) and width (red squares) with the light power. (b) Slope at the resonance point ($x = 0$) with the light power.

To check out the predictions given by Eqs. (8)–(11) with the optimal light power, we measure double-resonance signals for each heading angle of the DRAM and readout the absorptive A_{dc} , A_ω , and $A_{2\omega}$ component values on resonance ($x = 0$). The modulation of the rf frequency ω at low frequency ω_m is on when operated in M_z mode and is off when in M_x mode. The light linear polarization and the rf field are always parallel ($\varphi = \theta$). The experimental results show good agreement with the theoretical predictions, as shown in Fig. 4. We experimentally scan the heading angle more than 180° , which is enough for our dead-zone-free method, and theoretical fittings are in the range of 0° – 360° to show the whole period of the curves. From Fig. 4(a), one clearly sees that the absorptive component A_ω has a linear dependence on the heading angle θ (or φ) near 90° and can be used as an error signal to adjust and maintain the heading angle at 90° with respect to the bias field, which provides maximal amplitudes of $A_{2\omega}$ [$S_{2\omega}(t)$] and A_{dc} components as shown in Figs. 4(b) and 4(c), respectively. The angular range for the monotonous A_ω amplitude is about 72° – 108° . As we discuss above, the A_{dc} signal can be employed to realize a M_z magnetometer while the $S_{2\omega}(t)$ signal can be used in a M_x magnetometer.

To prove the feasibility of the dead-zone-eliminating method, we record the amplitudes of the A_{dc} and the $A_{2\omega}$ signals when rotating the direction of the bias field, as shown in Figs. 5(a) and 5(b), respectively. The rotation of the bias field is achieved with another set of two-dimensional coils. The blue circles present the amplitudes with open-loop control of the heading angle, and theoretical fits are based on Eqs. (10) and (11). Each data point is averaged from five measured results. The initial angles between the bias field and the light linear polarization (about 4.5°), between the bias field and the rf field

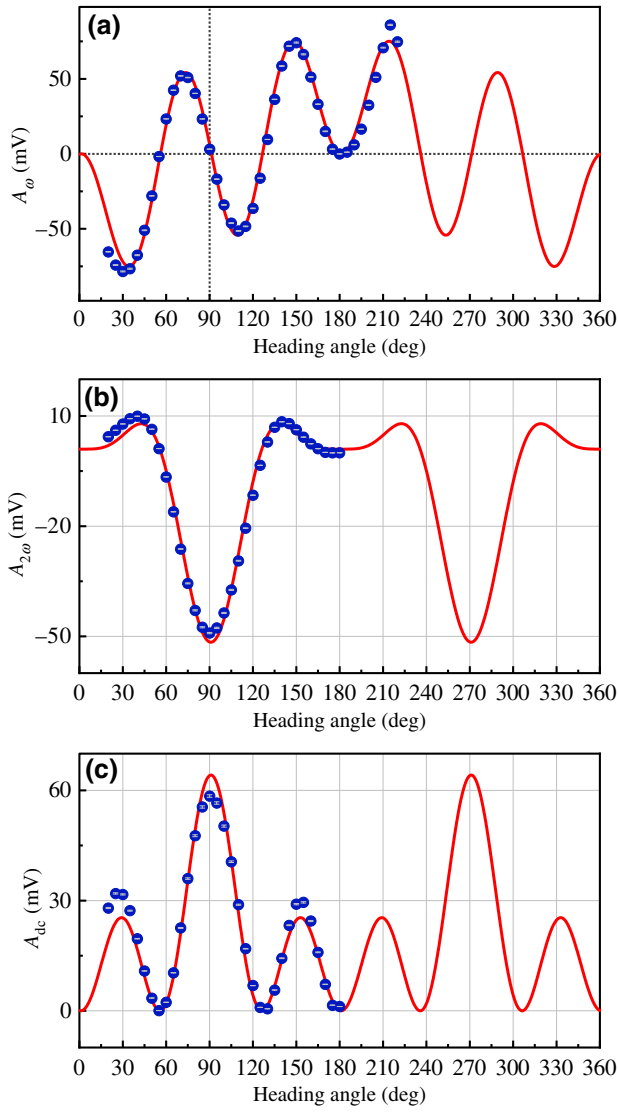


FIG. 4. Experimental (dots) and theoretical (lines) results for the angular dependence of A_ω , $A_{2\omega}$ and A_{dc} amplitudes on the heading angle θ (or φ). Theoretical fits are based on Eqs. (10) and (11). The light linear polarization is rotated by the polarization rotator and the rf field is controlled with the \mathbf{B}_1 coils shown in Fig. 2. The light linear polarization and the rf field are always parallel ($\varphi = \theta$, referred to as the heading angle). The error bar, which is smaller than the symbol size, shows the standard deviation of experimental data from five scans of the heading angle. (a) The amplitude of the A_ω signal. (b) The amplitude of the $A_{2\omega}$ signal. (c) The amplitude of the A_{dc} component in the S_0 signal.

(about 2°), are both taken into account in theoretical fits. From Figs. 5(a) and 5(b), we know that there are dead zones for both M_z and M_x signals. The red square symbols refer to the amplitudes when the heading angle is under controlled with a closed-loop control system (PID1 in Fig. 2) and the rf frequency is tracked on the Larmor frequency of the bias field in M_z mode (or in M_x mode)

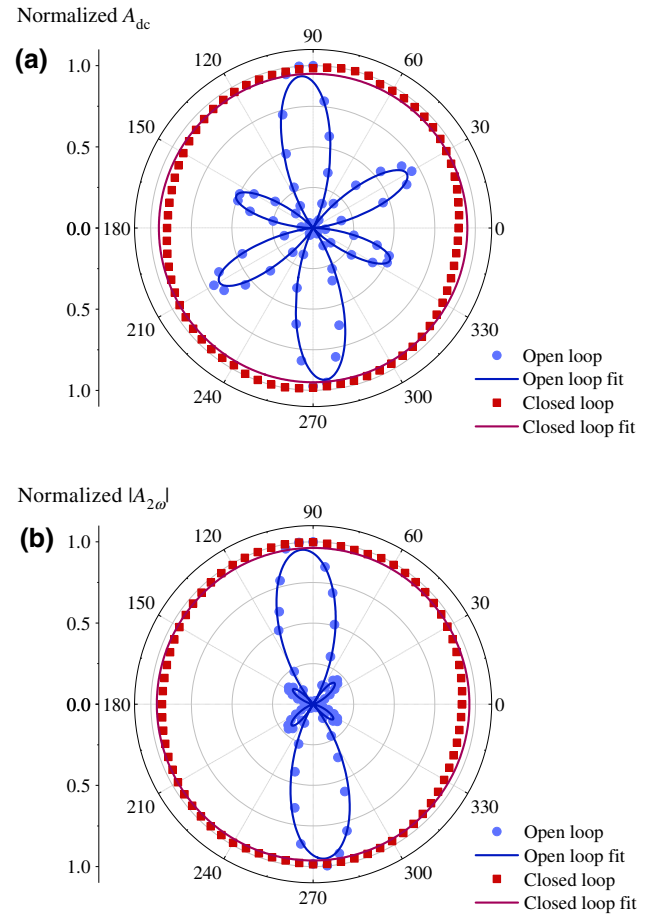


FIG. 5. Experimental (dots) and theoretical (lines) results for the polar diagram of the normalized resonance-signal amplitudes with the bias-field direction. The red squares and the blue circles refer to conditions whether the heading angle is under controlled or not, respectively. Theoretical fits of the blue circles are based on Eqs. (10) and (11), while the red squares are fitted with a constant. The slight angular deviation of the angle for maximal signal amplitudes from 90° is caused by the initial angles among the bias field, the light linear polarization, and the rf field, which are all taken into account in theoretical fits. (a) The normalized M_z signal amplitude (the amplitude of A_{dc}). (b) The normalized M_x second-harmonic signal amplitude (the absolute value of $A_{2\omega}$).

with a PID control system (PID2 in Fig. 2). The amplitudes, with closed-loop control of the heading angle, are normalized to the maximum value and the red lines are fitted with a constant. Here, the A_{dc} signal amplitude is represented by the amplitude of the signal demodulated at $2\omega_m$, which has a peak value when $x = 0$. The fluctuations of the A_{dc} and $A_{2\omega}$ signal amplitudes are within 10% with the heading angle under controlled when rotating the bias field around 360° , which is due to the control errors of the light linear polarization and the rf field. We can clearly see that the signal amplitudes of the M_z and M_x signals both keep its maximum value with varying magnetic field

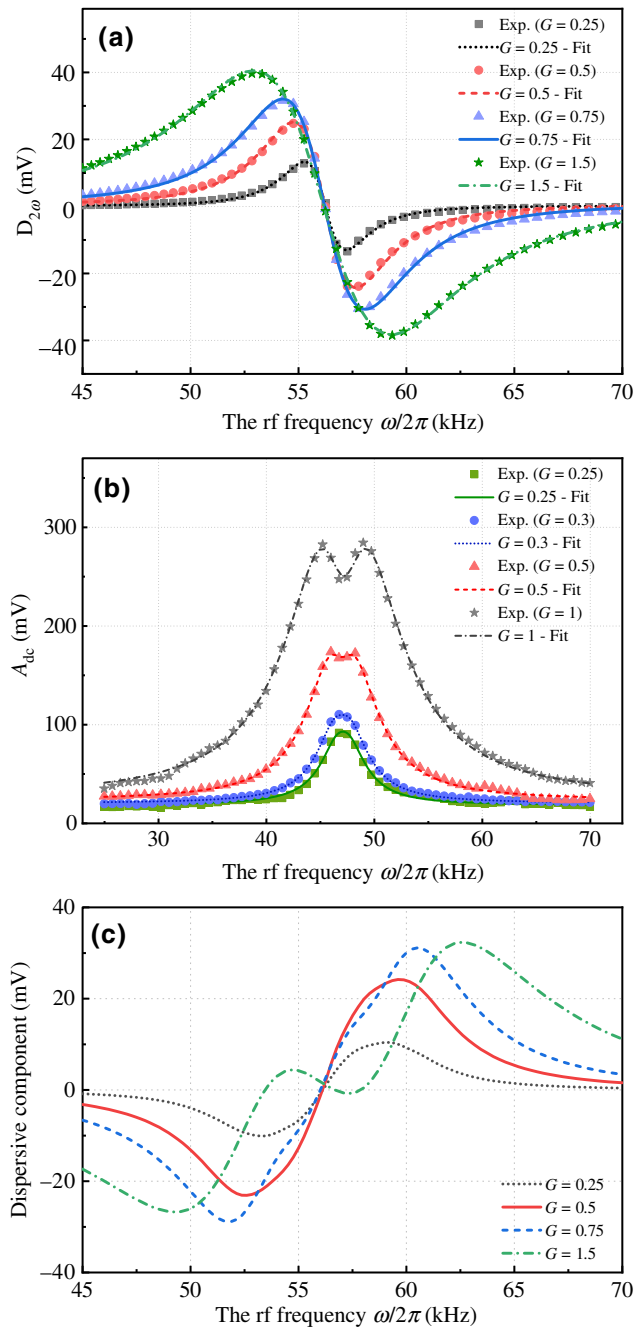


FIG. 6. Resonance signals for each rf amplitude (G). (a) Experimental (dots) and theoretical (lines) results for the M_x dispersive signals demodulated at 2ω ($D_{2\omega}$). (b) Experimental (dots) and theoretical (lines) results for the absorptive A_{dc} signals. (c) Experimental results for the M_z dispersive signals demodulated at ω_m . The modulation frequency ω_m is $2\pi \times 1.333$ kHz and the modulation depth is $2\pi \times 3$ kHz.

direction when the heading angle of the DRAM is under controlled, which proves that the dead-zone effect is eliminated with the feedback control system proposed in this paper and the DRAM can support isotropic measurement of the external magnetic field. In practical applications,

if the bias-field direction is unknown, one can rotate the heading angle around 180° and find the optimal heading angle where the A_{dc} and $A_{2\omega}$ signal amplitudes are maximal. Besides, the amplitude of the A_{dc} or $A_{2\omega}$ signal could be used as a monitor to check whether the heading angle is controlled properly.

The amplitude of the rf field is optimized for the control system and the sensitivity of the DRAM. For the control system, the slope at 90° when $x = 0$ is given by

$$\left. \frac{dA_\omega}{d\theta} \right|_{\theta=90^\circ} = \frac{3G}{2(1+4G^2)}. \quad (12)$$

One obtains a maximal slope to adjust the DRAM when $G = 0.5$. The PID1 feeds back into the polarization rotator and the \mathbf{B}_1 coils for the heading angle $\theta = \varphi = 90^\circ$, as shown in Fig. 2. For a given noise level of the demodulated signal and the fixed geometry $\theta = \varphi = 90^\circ$, the sensitivity of a magnetometer is determined by the slope of the dispersive signals on resonance ($x = 0$). For M_x magnetometers, the slope is given by

$$\left. \frac{dD_{2\omega}}{dx} \right|_{x=0} = \frac{9G^2}{4(G^2+1)(4G^2+1)}. \quad (13)$$

The maximal slope is achieved when $G = 0.7$ theoretically and $G \approx 0.75$ experimentally, as shown in Fig. 6(a). There is a slight trade-off between the maximal sensitivity of measuring the magnetic field and the most sensitive control system. A series of detailed studies on the line-shapes of M_x signals are presented previously [21,23,24], and we mainly focus on the M_z signal here. For M_z magnetometers, a reverse peak of A_{dc} signal will occur when $G > 0.35$, as seen in Fig. 6(b), which causes multiple zeros of the dispersive components, as shown in Fig. 6(c). Note that the $D_{2\omega}$ signal will not have multiple zeros when G is large, as shown in Fig. 6(a). The modulation parameters influence the lineshapes of the dispersive components in M_z magnetometers. In our experiment, the modulation frequency of the rf frequency is $2\pi \times 1.333$ kHz and the modulation depth is $2\pi \times 3$ kHz. Then, the slope of the dispersive component on resonance reaches its maximum when $G \approx 0.5$, as shown in Fig. 6(c), which is the optimum rf amplitude for obtaining the highest sensitivity of the M_z magnetometer and the most sensitive heading angle control system. The peak-to-peak frequency difference of the M_z dispersive resonance signal (linewidth) is about $2\pi \times 7$ kHz, which is broadened by the light field, the rf field and the frequency modulation, while the linewidth of the M_x dispersive resonance signal is about $2\pi \times 4$ kHz, which is broadened by the light field and the rf field.

In Figs. 7(a) and 7(b), the claimed sensitivity line drawn refers to the condition that the heading angle is under closed-loop control and is derived by taking fit of a band

of the power spectral density around 10 Hz and then taking its square root. To eliminate dead zones of the DRAM, the rf field should always be controlled to be parallel to the light linear polarization ($\theta = \phi$). Under this condition ($\theta = \phi$), the best sensitivity is reached when $\theta = \phi = 90^\circ$ for both M_z - [Fig. 7(a)] and M_x -mode [Fig. 7(b)] DRAMs. However, if we assume that the rf field direction and the light linear polarization are all arbitrarily oriented, the best sensitivity is reached when $\theta = \phi = 90^\circ$ for the M_x -mode DRAM [Fig. 7(b)], while that is reached when $\phi = 0^\circ$, $\theta = 90^\circ$ for the M_z -mode DRAM [Fig. 7(c)].

After parameter optimization, the dead-zone-free DRAM has a sensitivity of $0.9 \text{ pT}/\sqrt{\text{Hz}}$ at 10 Hz when operated in M_z mode, as shown in Fig. 7(a). The sensitivity is slightly smaller than reported isotropic optical magnetometers under intensity-modulated (sensitivity, $2 \text{ pT}/\sqrt{\text{Hz}}$) [22] or M_x configurations (sensitivity, $1 \text{ pT}/\sqrt{\text{Hz}}$) [19]. Besides, a magnetic field noise floor of $1.2 \text{ pT}/\sqrt{\text{Hz}}$ at 10 Hz is reached when the dead-zone-free DRAM is operated in M_x mode, as shown in Fig. 7(b). The slope of the M_x dispersive signal is about twice that of the M_z when $x = 0$. However, the noise floor of the M_x mode is somehow larger than the M_z mode even with the same experimental environment and parameter settings according to several experimental results. The additional noises could be attributed to phase fluctuations (e.g., from the cable and the instruments) since the M_x mode is sensitive to phase shifts. In addition, when the light polarization is parallel to the bias field ($\phi = 0^\circ$) and the rf field is perpendicular to the bias field ($\theta = 90^\circ$), the M_z -mode DRAM has a higher sensitivity than that with $\theta = \phi = 90^\circ$. Figure 7(c) shows the sensitivity of about $0.7 \text{ pT}/\sqrt{\text{Hz}}$ at 10 Hz in our experiment for the M_z -mode DRAM with the geometry $\phi = 0^\circ$ and $\theta = 90^\circ$, which may be useful in these situations that one does not need to use the dead-zone-eliminating method and wants to use the M_z -mode DRAM with the best sensitivity. We also present that the feedback system of the heading angle does not degrade the sensitivity of the DRAM whether in M_z mode or in M_x mode, which is shown in Figs. 7(a) and 7(b), respectively. The upper bound bandwidth of M_z magnetometers is limited by the relaxation rate Γ while that of M_x magnetometers can be beyond the relaxation rate Γ [20]. However, the output rate of the hardware system is 225 Hz, which limits the bandwidths of the two modes. The LIA is set with 100-Hz bandwidth and the parameters of the PID2 are also carefully adjusted to guarantee 100-Hz bandwidth.

In the absence of the technical noise, our magnetometer system is limited by the photon shot noise, which comes from the fluctuations of the photon number arriving at the photodiode. The photon-shot-noise-limited sensitivity can be obtained by the following equation [20]:

$$\delta B_{\text{SNL}} = \frac{k_F \rho_N \Gamma_{\text{MR}}}{\gamma R} \sqrt{f_b}, \quad (14)$$

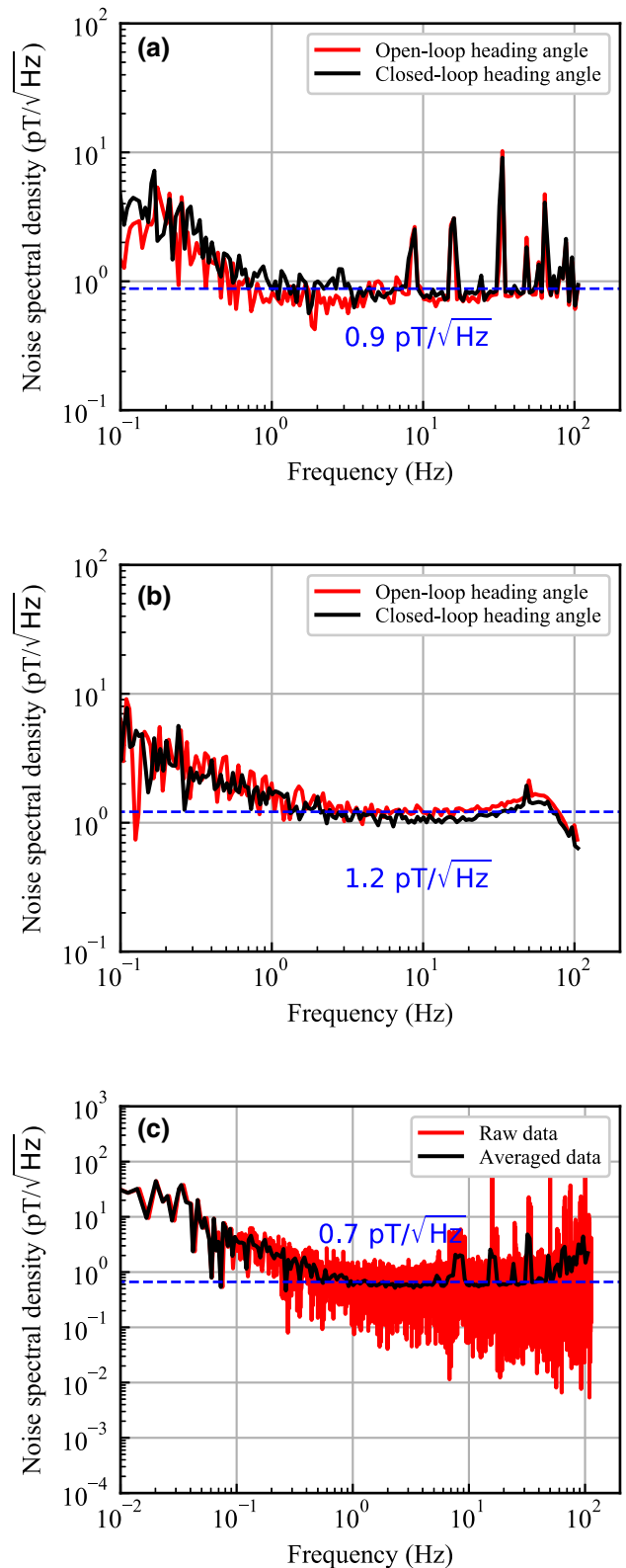


FIG. 7. Noise spectral density for the DRAM. (a),(b) are for the M_z -mode and M_x -mode DRAMs, respectively, whether the heading-angle control loop is closed (black) or open (red), and the geometry is kept to $\theta = \phi = 90^\circ$. (c) is for a M_z -mode DRAM operated with $\phi = 0^\circ$ and $\theta = 90^\circ$.

where $k_F = R/(\Gamma_{MR}S)$ is the resonance form factor, Γ_{MR} is the magnetic-resonance linewidth, R is the signal amplitude, S is the slope of the demodulated dispersive signal on resonance, ρ_N is the shot-noise spectral density, and f_b is the bandwidth, which usually corresponds to the measurement time t_m . The average photon number can be calculated as Pt_m/E_p for the measuring time t_m , where E_p is the photon energy, P is the light power. The photon shot noise is assumed to be white noise. In our experiment, $\gamma = 2\pi \times 28.025$ Hz/nT is the gyromagnetic ratio of the ^4He metastable state, the light power is about 3.5 mW, the measuring time is about 5 ms, and the bandwidth is about 100 Hz. Then the photon-shot-noise-limited sensitivity of the DRAM in M_z mode is about 90 fT/ $\sqrt{\text{Hz}}$, while that of the M_x mode is about 40 fT/ $\sqrt{\text{Hz}}$, when the heading angle is under controlled ($\theta = \phi = 90^\circ$). In addition, the δB_{SNL} of the M_z -mode DRAM with the special geometry $\phi = 0^\circ$ and $\theta = 90^\circ$ is about 45 fT/ $\sqrt{\text{Hz}}$. However, this configuration ($\phi = 0^\circ$ and $\theta = 90^\circ$) suffers from the dead-zone effect.

In addition, to eliminate the dead zones, our proposal also strongly suppresses the heading errors in principle. The heading-error effect is that the output values of OPMs depend on the relative orientation of the sensor with respect to the bias field. The light linear polarization and the rf field are fixed to be perpendicular to the bias field in our proposal. Besides, the ^4He atoms without nuclear spin are free from the nonlinear Zeeman splitting [35]. The employment of linearly polarized light is helpful to reduce heading errors caused by the vector light shifts [36]. The nonlinear Zeeman splitting and vector light shifts are two main sources of heading errors in OPMs operated in the geophysical field range [37]. Considering the control errors of the angles θ , ϕ and the fact that the linearly polarized light is not perfect, the heading errors of the DRAM should be calibrated experimentally. However, limited by the control precision of the rotating bias field [38], the heading errors are hard to calibrate precisely. The control precision is greatly influenced by the residual background field remaining inside the magnetic shield and the calibration errors of the two-dimensional coils to produce the rotating bias field. Future experimental work will focus on developing an integrated sensor and rotating the sensor in a static magnetic field to calibrate its heading errors accurately.

IV. CONCLUSION

In conclusion, we present analytical expressions for the full spectra produced by a DRAM in arbitrary magnetic field geometries. We propose and optimize a method to realize a dual-mode single-beam dead-zone-free DRAM by synchronously adjusting and maintaining the light linear polarization and the rf field to be perpendicular to the bias field to be measured. The M_x and M_z modes usually have different sensitivities. Only one mode could be used

to measure the bias field at the same time. Whether in M_x or M_z mode, the sensitivity of the dead-zone-free DRAM is independent of magnetic field directions. The single-beam isotropic DRAM has a sensitivity of 0.9 pT/ $\sqrt{\text{Hz}}$ and 1.2 pT/ $\sqrt{\text{Hz}}$ at 10 Hz in M_z and M_x modes, respectively. Besides, the fixed geometry of the sensor with respect to the bias field, and the employment of metastable ^4He atoms and linearly polarized light can, in principle, reduce the heading errors. Our approach is suitable for applications where isotropic measurement of the external magnetic field is required, such as in mobile applications with varying magnetic field directions. Future work will concentrate on two main aspects. One is to improve the sensitivity through optimizing the linewidths of resonance signals, the laser frequency and intensity stabilization systems, and the power stability of the rf discharge that produces the metastable ^4He atoms. The other is to push forward the progress of the integration of the isotropic DRAM, and bring the portable DRAM into practical applications without loss of sensitivity.

ACKNOWLEDGMENTS

The authors thank R. Zhang for useful discussions and S. Li for comments on the draft of the paper. This work is supported by the National Natural Science Foundation of China (Grants No. 62071012, No. 61571018 and No. 61531003).

-
- [1] I. Kominis, T. Kornack, J. Allred, and M. V. Romalis, A subfemtotesla multichannel atomic magnetometer, *Nature* **422**, 596 (2003).
 - [2] D. Sheng, S. Li, N. Dural, and M. V. Romalis, Subfemtotesla Scalar Atomic Magnetometry Using Multipass Cells, *Phys. Rev. Lett.* **110**, 160802 (2013).
 - [3] D. Budker and M. Romalis, Optical magnetometry, *Nat. Phys.* **3**, 227 (2007).
 - [4] E. Boto, N. Holmes, J. Leggett, G. Roberts, V. Shah, S. S. Meyer, L. D. Muñoz, K. J. Mullinger, T. M. Tierney, S. Bestmann, G. R. Barnes, R. Bowtell, and M. J. Brookes, Moving magnetoencephalography towards real-world applications with a wearable system, *Nature* **555**, 657 (2018).
 - [5] R. Zhang, W. Xiao, Y. Ding, Y. Feng, X. Peng, L. Shen, C. Sun, T. Wu, Y. Wu, Y. Yang, Z. Zheng, X. Zhang, J. Chen, and H. Guo, Recording brain activities in unshielded Earth's field with optically pumped atomic magnetometers, *Sci. Adv.* **6**, eaba8792 (2020).
 - [6] M. E. Limes, E. L. Foley, T. W. Kornack, S. Caliga, S. McBride, A. Braun, W. Lee, V. G. Lucivero, and M. V. Romalis, Portable Magnetometry for Detection of Biomagnetism in Ambient Environments, *Phys. Rev. Appl.* **14**, 011002 (2020).
 - [7] M. S. Safronova, D. Budker, D. DeMille, D. F. Jackson Kimball, A. Derevianko, and C. W. Clark, Search for new

- physics with atoms and molecules, *Rev. Mod. Phys.* **90**, 025008 (2018).
- [8] C. Abel *et al.*, Measurement of the Permanent Electric Dipole Moment of the Neutron, *Phys. Rev. Lett.* **124**, 081803 (2020).
- [9] N. Olsen, G. Hulot, V. Lesur, C. C. Finlay, C. Beggan, A. Chulliat, T. J. Sabaka, R. Floberghagen, E. Friis-Christensen, and R. Haagmans, The swarm initial field model for the 2014 geomagnetic field, *Geophys. Res. Lett.* **42**, 1092 (2015).
- [10] A. Balogh, Planetary magnetic field measurements: Missions and instrumentation, *Space Sci. Rev.* **152**, 23 (2010).
- [11] K.-M. C. Fu, G. Z. Iwata, A. Wickenbrock, and D. Budker, Sensitive magnetometry in challenging environments, *AVS Quantum Sci.* **2**, 044702 (2020).
- [12] B. Chéron, H. Gilles, and J. Hamel, Spatial frequency isotropy of an optically pumped ^4He magnetometer, *Eur. Phys. J. Appl. Phys.* **13**, 143 (2001).
- [13] M. K. Plante, D. L. MacFarlane, D. D. McGregor, R. E. Slocum, W. M. Sampson, and A. W. Brown, Generalized theory of double-resonance optical pumping of ^4He , *Phys. Rev. A* **82**, 013837 (2010).
- [14] A. Ben-Kish and M. V. Romalis, Dead-Zone-Free Atomic Magnetometry with Simultaneous Excitation of Orientation and Alignment Resonances, *Phys. Rev. Lett.* **105**, 193601 (2010).
- [15] G. Bevilacqua and E. Breschi, Magneto-optic spectroscopy with linearly polarized modulated light: Theory and experiment, *Phys. Rev. A* **89**, 062507 (2014).
- [16] H. Wang, T. Wu, H. Wang, X. Peng, and H. Guo, Magneto-optical spectroscopy with arbitrarily polarized intensity-modulated light in ^4He atoms, *Phys. Rev. A* **101**, 063408 (2020).
- [17] C. Guttin, J. Léger, and F. Stoeckel, An isotropic earth field scalar magnetometer using optically pumped helium 4, *J. Phys. IV* **4**, C4 (1994).
- [18] J. Rutkowski, W. Fourcault, F. Bertrand, U. Rossini, S. Gétin, S. Le Calvez, T. Jager, E. Herth, C. Gorecki, and M. Le Prado *et al.*, Towards a miniature atomic scalar magnetometer using a liquid crystal polarization rotator, *Sens. Actuators A* **216**, 386 (2014).
- [19] G. Hulot, J.-M. Léger, P. Vigneron, T. Jager, F. ois Bertrand, P. Coisson, P. Deram, A. Boness, L. Tomasini, and B. Faure, in *IEEE Int. Geosci. and Remote Sens. Symp. (IGARSS)* (IEEE, Valencia, 2018), p. 6320.
- [20] E. B. Alexandrov and A. K. Vershovskiy, in *Optical Magnetometry*, edited by D. Budker and D. F. Jackson Kimball (Cambridge University, Cambridge, 2013), p. 60.
- [21] A. Weis, G. Bison, and Z. D. Grujić, in *High Sensitivity Magnetometers*, edited by A. Grosz, M. J. Haji-Sheikh, and S. C. Mukhopadhyay (Springer, Cham, 2017), p. 361.
- [22] T. Wu, X. Peng, Z. Lin, and H. Guo, A dead-zone free ^4He atomic magnetometer with intensity-modulated linearly polarized light and a liquid crystal polarization rotator, *Rev. Sci. Instrum.* **86**, 103105 (2015).
- [23] A. Weis, G. Bison, and A. S. Pazgalev, Theory of double resonance magnetometers based on atomic alignment, *Phys. Rev. A* **74**, 033401 (2006).
- [24] G. Di Domenico, G. Bison, S. Groeger, P. Knowles, A. S. Pazgalev, M. Rebetz, H. Saudan, and A. Weis, Experimental study of laser-detected magnetic resonance based on atomic alignment, *Phys. Rev. A* **74**, 063415 (2006).
- [25] G. Di Domenico, H. Saudan, G. Bison, P. Knowles, and A. Weis, Sensitivity of double-resonance alignment magnetometers, *Phys. Rev. A* **76**, 023407 (2007).
- [26] S. J. Ingleby, C. O'Dwyer, P. F. Griffin, A. S. Arnold, and E. Riis, Vector Magnetometry Exploiting Phase-Geometry Effects in a Double-Resonance Alignment Magnetometer, *Phys. Rev. Appl.* **10**, 034035 (2018).
- [27] Z. Lin, H. Wang, X. Peng, T. Wu, and H. Guo, Laser pumped ^4He magnetometer with light shift suppression, *Rev. Sci. Instrum.* **87**, 115111 (2016).
- [28] P. D. D. Schwindt, B. Lindseth, S. Knappe, V. Shah, J. Kitching, and L.-A. Liew, Chip-scale atomic magnetometer with improved sensitivity by use of the M_x technique, *Appl. Phys. Lett.* **90**, 081102 (2007).
- [29] D. Budker, W. Gawlik, D. F. Jackson Kimball, S. M. Rochester, V. V. Yashchuk, and A. Weis, Resonant nonlinear magneto-optical effects in atoms, *Rev. Mod. Phys.* **74**, 1153 (2002).
- [30] W. Happer, Optical pumping, *Rev. Mod. Phys.* **44**, 169 (1972).
- [31] G. Le Gal, G. Lieb, F. Beato, T. Jager, H. Gilles, and A. Palacios-Laloy, Dual-Axis Hanle Magnetometer Based on Atomic Alignment with a Single Optical Access, *Phys. Rev. Appl.* **12**, 064010 (2019).
- [32] G. Bevilacqua, E. Breschi, and A. Weis, Steady-state solutions for atomic multipole moments in an arbitrarily oriented static magnetic field, *Phys. Rev. A* **89**, 033406 (2014).
- [33] T. Wu, X. Peng, W. Gong, Y. Zhan, Z. Lin, B. Luo, and H. Guo, Observation and optimization of ^4He atomic polarization spectroscopy, *Opt. Lett.* **38**, 986 (2013).
- [34] F. Beato and A. Palacios-Laloy, Second-order effects in parametric-resonance magnetometers based on atomic alignment, *EPJ Quantum Technol.* **7**, 1 (2020).
- [35] G. Bao, A. Wickenbrock, S. Rochester, W. Zhang, and D. Budker, Suppression of the Nonlinear Zeeman Effect and Heading Error in Earth-Field-Range Alkali-Vapor Magnetometers, *Phys. Rev. Lett.* **120**, 033202 (2018).
- [36] H. Wang, C. Du, H. Wang, M. Xia, X. Peng, and H. Guo, Aeromagnetic compensation with suppressing heading error of the scalar atomic magnetometer, *IEEE Geosci. Remote Sens. Lett.* **17**, 1134 (2020).
- [37] G. Oelsner, V. Schultze, R. IJsselsteijn, F. Wittkämper, and R. Stolz, Sources of heading errors in optically pumped magnetometers operated in the Earth's magnetic field, *Phys. Rev. A* **99**, 013420 (2019).
- [38] S. J. Ingleby, P. F. Griffin, A. S. Arnold, M. Chouliara, and E. Riis, High-precision control of static magnetic field magnitude, orientation, and gradient using optically pumped vapour cell magnetometry, *Rev. Sci. Instrum.* **88**, 043109 (2017).